JACS
JOURNAL OF THE AMERICAN CHEMICAL SOCIETY

ARTICLE

pubs.acs.org/JACS

Single Atom Hot-Spots at Au−Pd Nanoalloys for Electrocatalytic H_2O_2 Production

Jakub S. Jirkovský,[*,†,#] Itai Panas,[*,‡] Elisabet Ahlberg,[§] Matej Halasa,[∥] Simon Romani,[⊥] and David J. Schiffrin[†]

[†]Chemistry Department, University of Liverpool, Liverpool L69 7ZD, United Kingdom

[‡]Department of Chemistry and Biotechnology, Chalmers University of Technology, SE-412 96, Gothenburg, Sweden

[§]Department of Chemistry, University of Gothenburg, SE-412 96, Gothenburg, Sweden

[∥]Solvay R&D, rue de Ransbeek 310, 1120 Brussels, Belgium

[⊥]Centre for Materials and Structures, University of Liverpool, Liverpool L69 3GH, United Kingdom

Supporting Information

ABSTRACT: A novel strategy to direct the oxygen reduction reaction to preferentially produce H_2O_2 is formulated and evaluated. The approach combines the inertness of Au nanoparticles toward oxidation, with the improved O_2 sticking probability of isolated transition metal "guest" atoms embedded in the Au "host". DFT modeling was employed to screen for the best alloy candidates. Modeling indicates that isolated alloying atoms of Pd, Pt, or Rh placed within the Au surface should enhance the H_2O_2 production relative to pure Au. Consequently, $Au_{1-x}Pd_x$ nanoalloys with variable Pd content supported on Vulcan XC-72 were prepared to investigate the predicted selectivity toward H_2O_2 production for Au alloyed with Pd. It is demonstrated that increasing the Pd concentration to 8% leads to an increase of the electrocatalytic H_2O_2 production selectivity up to nearly 95%, when the nanoparticles are placed in an environment compatible with that of a proton exchange membrane. Further increase of Pd content leads to a drop in H_2O_2 selectivity, to below 10% for $x = 0.5$. It is proposed that the enhancement in H_2O_2 selectivity is caused by the presence of individual surface Pd atoms surrounded by gold, whereas surface ensembles of contiguous Pd atoms support H_2O formation. The results are discussed in the context of exergonic electrocatalytic H_2O_2 synthesis in Polymer Electrolyte Fuel Cells for the simultaneous cogeneration of chemicals and electricity, the latter a credit to production costs.

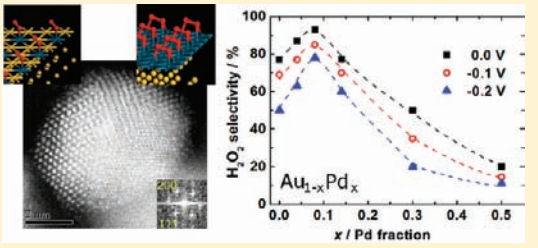

INTRODUCTION

Hydrogen peroxide is an important chemical produced in large scale with many applications including the pulp and paper industry, disinfection,[1] many consumer goods, and recently, industrial synthesis of propylene oxide.[2] H_2O_2 is manufactured by the anthraquinone process[1] requiring large production plants to minimize capital investment and to obtain concentrated H_2O_2 to reduce transportation costs. For most applications, however, dilute hydrogen peroxide is appropriate and a less energy demanding synthetic technology with the possibility of local production units is highly desirable.[3]

An attractive production strategy would employ the concept of cogeneration of chemicals and electrical energy. In chemical transformations, a proportion of the Gibbs energy driving the reaction is lost and its utilization, if possible, would represent a significant credit to production costs. An important example of a process in which these ideas could be applied is the industrial production of hydrogen peroxide, an intermediate in the electrochemical oxygen reduction reaction.[4] Polymer Electrolyte Fuel Cells (PEFC) are ideally suited for this strategy provided suitable electrocatalysts can be found to stop further reduction of the intermediate peroxide to yield water. Previous examples employing classical electrolysis cells and using hydrogen anodes for producing H_2O_2 in strong alkaline solutions have been described,[5] but this requires difficult and unworkable separations for the synthesis of pure H_2O_2.

PEFCs employing proton exchange membrane (PEM) electrolytes allows high current densities, and therefore, this technology is considered as promising for replacing current internal combustion engines. PEFCs for traction applications produce water as the final product of the reaction between hydrogen and oxygen and hydrogen peroxide is regarded as an undesirable byproduct that decreases energy output.[6] The present work aims at developing a general methodology for the rational design of appropriate catalysts that would allow turning the current strategies for the development of PEFCs upside down to greatly enlarge their range of applications by including clean industrial syntheses.[7] Thus, the use of PEFCs would allow the production of H_2O_2 due to the high current density achievable by this technology at low operational temperatures. Other possible reactions of industrial importance that could be amenable to this approach are the syntheses of propylene and ethylene oxides, although the corresponding electrochemistry is far less

Received: July 12, 2011
Published: October 25, 2011

ACS Publications © 2011 American Chemical Society

Table 1. Characterization of Prepared Materials

material	Pd content/ mol %	particles diameter (TEM)/nm	particles diameter (XRD)/nm	loading (AuPd)/ C/ w/w-%	$A_S/m^2\ g^{-1}$	metal (Au + Pd) loading at electrode/$\mu g\ cm^{-2}$
Au/C	0	5.6 ± 1.2	5.7	8.0	5.5	99
$Au_{0.96}Pd_{0.04}/C$	4	5.8 ± 1.2	6.0	8.3	5.5	103
$Au_{0.92}Pd_{0.08}/C$	8	6.0 ± 1.5	6.0	8.9	5.7	110
$Au_{0.85}Pd_{0.15}/C$	15	8.1 ± 2.1	8.5	9.3	5.6	116
$Au_{0.7}Pd_{0.3}/C$	30	8.7 ± 2.5	9.0	10.5	5.8	130
$Au_{0.5}Pd_{0.5}/C$[a]	50	6.8 ± 2.2	11.0	14	8.5	174

[a] This material was prepared by a different synthetic method described, e.g., in ref 28 (AuPd(sol) method). The compositional Au−Pd ratios were calculated from the results of the ICP analysis. A_S refers to the surface area of Au−Pd alloy with respect to one gram of the Au−Pd/C catalyst and was calculated as described in ref 17.

developed than that of H_2O_2.[8] The electrochemical engineering already developed for PEFCs can be transposed for its use in cogeneration operations allowing the Gibbs energy of the O_2 to H_2O_2 conversion as well as losses due to H_2O formation as a side product to be recycled as electrical energy. This represents the main difference with the *direct chemical* synthesis of H_2O_2[3,9] for which the Gibbs energy of the reaction is not fully employed. In addition, PEFCs offers a safety benefit by employing well-separated H_2 and O_2 reaction streams.

Current PEFC technology requires electrocatalysts suitable for use in acid media.[6] Although quinones have been shown to be highly effective to quantitatively convert oxygen to H_2O_2,[10] their application is restricted to an alkaline environment, precluding their use with the currently available proton exchange membrane technology.[11] PEM fuel cell engineering is well established and the development of a highly selective electrocatalyst for H_2O_2 production in acid media would represent a major step toward a new industrial synthetic technology.

Only a few electrocatalytic materials show suitable stability in acid media. Gold supports both the H_2O_2 and H_2O oxygen reduction pathways depending on crystallographic orientation and experimental conditions.[12,13] Two main reduction mechanisms, reflecting the most commonly encountered coordination chemistry of O_2 have been considered:[14,15]

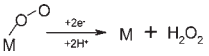

(I)

and

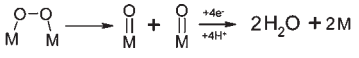

(II)

that is, an end-on and a μ-peroxo coordination. Reaction (II) is not, however, the only channel leading to water and reaction (III) can represent another important pathway:

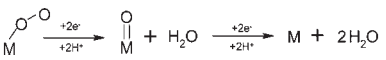

(III)

It has been known for a long time that some transition metals such as cobalt, when present in a macrocyclic complex, can give rise to high yields of peroxide, mainly following reaction (I).[16] However, such materials suffer long-term degradation and a preferred choice is to attempt to reproduce the same reduction mechanism but avoiding the decay route indicated by reaction (II) by using alloys. In the present work, an electroactive surface containing *discrete* transition metal reaction centers present in a low concentration of an alloy with gold is employed. Gold was chosen as the host since O_2 reduction on Au nanoparticles in a fuel cell compatible environment is known to produce good yields of H_2O_2.[17] It was expected that by a rational design of alloying components and composition, product distribution could be directed to avoid O−O bond breaking during the reduction process, a problem that has received attention for a long time for the industrial direct synthesis of H_2O_2, from O_2 and H_2.[18] More recently, extensive work by Hutchings et al. have investigated the Pd−Au system as an heterogeneous catalyst for producing good yields of hydrogen peroxide.[3,9,19]

The concept of individual atomic sites as reaction centers presented in this paper represents a new approach in electrocatalysis for the oxygen reduction reaction. So far, predictions of electrocatalytic reactivity have been based mainly on the so-called volcano plots.[20,21] These predictions, however, assume an homogeneous distribution of reactant/product binding energies, for instance, over an alloy surface, and therefore have been described by the d-band center of the metal. A multicomponent surface, however, implies different interaction energies between reactant/products and individual atoms within the surface.[22,23] Except for CO oxidation, the impact of these phenomena, also known as ensemble effects, has received little attention in electrocatalysis, although the work by Pluntke et al.,[24] that reported enhanced hydrogen evolution on Pd monomers at a Au surface, suggests their general importance. In this case, the highest activity for the hydrogen evolution reaction was observed for low Pd coverage at a Au (111) surface,[25,26] as well as for the hydrogen oxidation reaction,[26] although different Au−Pd surface ensembles appeared to be beneficial for these reactions.

The purpose of the present work was to establish a robust methodology for electrocatalyst design and for the selection of alloying metals for incorporation into a gold matrix to direct reactivity in favor of reaction (I). The paper is divided in three sections. First, the idea of individual metal centers and use of Density Functional Theory (DFT) to screen possible candidates to achieve high selectivity in the reduction of oxygen to hydrogen peroxide is introduced. Second, the synthesis and characterization of the nanoalloys employed in the preparation of electrodes to test theoretical predictions is described. Finally, their electrochemical properties are measured and analyzed and the implications of the methodology to develop further the concept of cogeneration of electrical energy and chemicals are discussed.

METHODS

Chemicals. Hydrolyzed poly(vinyl alcohol), 98%, average molecular weight of 16000 g/mol, was purchased from Acros Organics. Sodium

borohydride (99.9%), hydrogen tetrachloroaurate(III) trihydrate (99.9%), palladium(II) chloride (99.9%), and redistilled $HClO_4$ (99.999%) 70% were supplied by Aldrich. Oxygen (99.95%), argon (99.997%), and 10% H_2/90%Ar mixture were obtained from BOC gases (U.K.). Milli-Q water (Millipore, Inc.) was used in all experiments. XC-72R carbon black (Cabot Corporation) was used as electrocatalyst support and purified as described in ref 17.

Electrocatalysts. The $Au_{1-x}Pd_x/C$ catalysts were prepared by a sequential reduction synthetic method.[27] To study the effect of different concentrations of Pd active sites incorporated in the Au nanoalloys, the same Au/C base matrix[17] was used for the preparation of the nanoalloys, and the Pd content varied. A 32 μg/mL $HAuCl_4$ aqueous solution containing poly(vinyl alcohol) (PVA) (Au/PVA in 2:1 weight ratio) was reduced by adding dropwise a 4-fold excess of 0.1 M $NaBH_4$ with vigorous stirring. The Au colloidal solution obtained was then added to a vigorously stirred suspension of carbon black in water prepared by dispersing carbon in 200 mL of water in an ultrasonic bath (60 min). The dispersion was kept stirred for another hour and then the carbon supported catalyst was left to settle overnight. The solution was decanted and the solid residue was collected, washed with water, and centrifuged several times. The material obtained was first dried in air at 60 °C and then annealed for 6 h under a stream of 10% H_2/90% Ar at 300 °C. The solid obtained was then redispersed in water in an ultrasonic bath (1 h) and appropriate amounts of $PdCl_2$ solution were added in order to prepare $Au_{1-x}Pd_x/C$ electrocatalysts with different values of x between 0 and 0.5, as summarized in Table 1. The reduction of the Pd(II) salt was achieved by bubbling H_2 through the suspension for 1 h. The materials obtained were separated by centrifugation, washed with water several times, and finally dried in air at 60 °C.

Materials Characterization. TEM images and EDX data were obtained with a JEOL 2000FX and JEOL3010 transmission electron microscopes with acceleration voltages of 200 and 300 kV, respectively. A JEM 2100F Field Emission Gun Transmission Electron Microscope (FEG TEM) equipped with a CEOS probe aberration corrector was used for ultra high resolution and HAADF analysis. The powder XRD patterns were obtained on a PANalytical X'pert pro Multi-Purpose diffractometer (Co Kα_1 radiation). The average crystallite size was estimated using the Scherrer formula:

$$D_h = \frac{\lambda}{\beta_h \cos \theta_i} \quad (1)$$

D_h is the volume-weighted domain size of the diffraction line, λ is the wavelength of the Co source used (1.788965 Å); β_i is the width in radians of the diffraction peak measured at half-maximum intensity (fwhm) and corrected for instrumental broadening and θ_i is the angle of the particular *hkl* reflection. The actual loading of Au and Pd was determined using an ICP-AES spectrometer (Ciros, Spectro, US). The samples were digested with Aqua Regia.

Electrochemical Measurements. For the rotating ring-discc electrode (RRDE) experiments, a Pine Instrument Company glassy carbon (GC)/Pt disc−ring electrode of 0.247 cm^2 disc area was employed. The ring potential was set at 1.0 V to ensure quantitative detection of the peroxide produced on the disc. A collection efficiency of 0.4 was determined from measurements of hexacyanoferrate(III) reduction. The electrode was rotated using a Pine Instrument Company (Grove City, PA) FMSRX rotator and MSRX speed controller. The electrochemical experiments were performed in a single compartment cell with controlled atmosphere and temperature (293.15 K). The applied potential was controlled with an Eco Chemie Autolab potentiostat (The Netherlands) and the measurements were carried out in a three electrode cell arrangement. A saturated calomel electrode (SCE) was used as the reference electrode (+0.3 V vs reversible hydrogen electrode (RHE) in 0.1 M $HClO_4$) and a gold wire as counter electrode. An Ar or O_2 saturated 0.1 M $HClO_4$ aqueous solution was used as electrolyte for all the measurements.

The electrodes were prepared as previously described.[17] Typically, 10 mg of carbon supported catalyst, 2.25 mL of water, and 0.25 mL of 5% Nafion 117 solution (Fluka) were mixed in an ultrasonic bath. The GC disc was polished to a mirror finish using increasingly finer aqueous alumina slurries (1.0, 0.3, and 0.05 mm, Buehler) prior to each experiment, followed by repeated sonication in water. The electrodes were prepared by placing 12 μL of the catalyst suspension on the glassy carbon electrode and then left to evaporate overnight. An electrocatalytic layer with thickness of ~1 μm was calculated from the $Au_{1-x}Pd_x/C$ and Nafion loadings and densities.[17] The homogeneity of the layer was checked by observation with an optical microscope and electrochemically, from the reproducibility of the O_2 reduction experiments.

Computational Details. The periodic boundary conditions version of DMol3 code[29,30] as implemented on the Materials Studio platform[31] was employed throughout. A three atomic layer slab representing a (111) surface was employed as a model framework for screening the properties of different guest atoms embedded within a Au matrix. The supercell was composed of 4 × 2 surface elementary unit cells. A 15 Å thick vacuum space separated the slab in the vertical direction. For the investigated surfaces composed of guest atom monomers, the guest atom coverage was 0.125 ML. All calculations were performed at the GGA PBE[32] level of theory using a double-Zeta numerical basis set with polarization functions on the hydrogen (DNP). A 3 × 2 × 1 k-point sampling was employed for the Brillouin zone integration. The core electrons were approximated by semilocal pseudopotentials.[33] In all calculations, the bottom layer was frozen in the crystal structure configuration and only two top-layers were allowed to relax in response to the surface chemistry. All the calculations compare the reactivity of the guest−host systems with that of a pure gold (111) surface. The results of the calculations establish differences in the stability of O_2(ads) and HO_2(ads), as well as differential reactivities toward fragmentation of HO_2(ads). All the calculations reflect electroneutral adsorption and hydrogenation of molecular O_2.

RESULTS AND DISCUSSION

Theoretical Analysis. The modeling approach followed relies on placing 'guest' transition metals atoms within a Au host matrix as a dilute alloy at a concentration such that the average distance between two neighboring guest transition metal atom centers would not be expected to allow mechanism (II) to proceed. The presence of such surface structures is experimentally demonstrated below. The unusual catalytic properties of single surface atoms in a noncatalytic matrix have been previously reported.[34] In the present work, the effect of alloying on the O_2 chemistry on model surfaces where a single Au host atom within an Au(111) surface is replaced by various transition metal guest atoms, that is, Co, Ni, Cu, Zn, Rh, Pd, Ir, and Pt, has been investigated.

Reactivity for O_2 Reduction of Discrete Centers M at a Au (111) Surface. To establish the impact of alloying on the interactions of the modified surface with oxygenated species, DFT modeling was referred in all cases to those obtained for a surface where gold is both the host and the 'guest'. Such comparative study is expected to reflect mainly chemical interactions involving the different atoms incorporated within the Au lattice whereas possible strain effects due to differences in atomic size are of secondary importance.[23] Calculations were performed for two situations. The first one considers the differences in coordination of O_2(ads) and O_2H(ads) between Au and the metal M, both present within the same surface environment. In the second, the reduction channel leading to H_2O, that is, reactions (II) and (III) involving O−O bond breaking by the

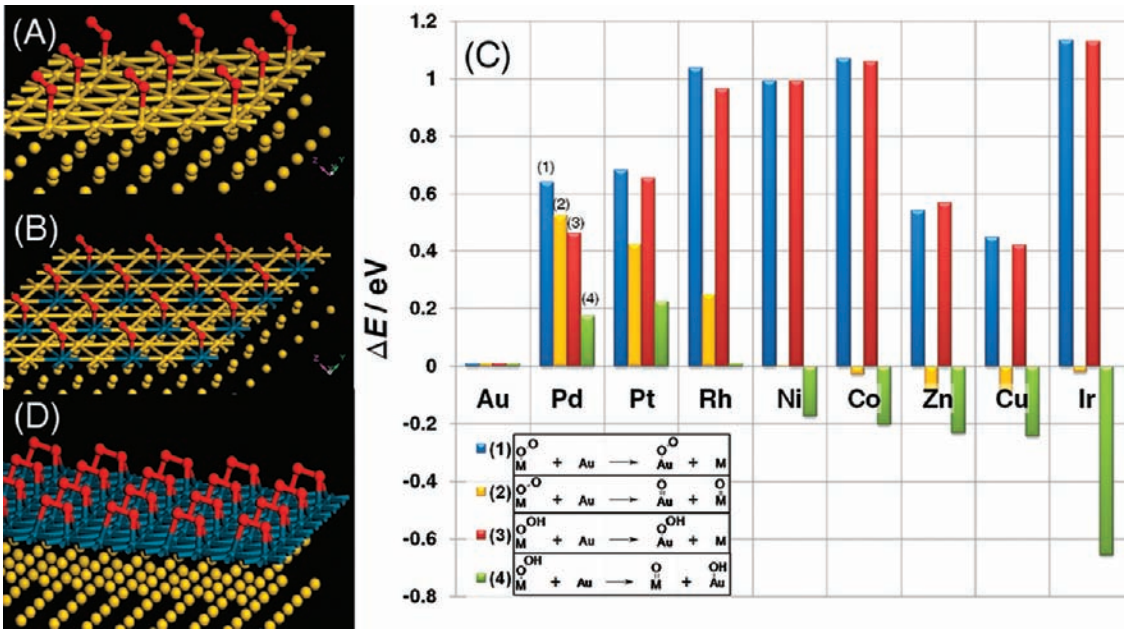

Figure 1. DFT analysis of O_2 reduction on Au−M alloys. (A) Adsorption of O_2 (red) on Au (111) (yellow) and (B) on metal M atoms (blue) incorporated in a Au(111) matrix. (C) Differences in adsorption energy and O−O bond dissociation energies on pure Au (111) and metal M centers incorporated in this surface for −OO(ads) and −OOH (ads) species. (D) O_2 adsorption on a Pd monolayer (blue) present on top of a Au (111) surface.

Table 2. Calculated Energy Differences

M	(IV) OOM + Au → M + OOAu/eV	(V) OOM + Au → OM + OAu/eV	(VI) HOOM + Au → M + HOOAu/eV	(VII) HOOM + Au → OM + HOAu/eV	(VIII) H_2O_2 + M → H_2O + OM/eV
Au	0	0	0	0	−0.656
	(0)[a]	(−0.0785)[a]	(0)[a]	(−0.473)[a]	
Pd	0.641	0.5225	0.462	0.175	−1.040
Pt	0.683	0.4235	0.654	0.225	
Rh	1.036	0.2495	0.965	0.01	
Ni	0.993	0.0015	0.993	−0.173	
Co	1.07	−0.0285	1.06	−0.203	
Zn	0.54	−0.0915	0.568	−0.232	
Cu	0.448	−0.0915	0.421	−0.243	
Ir	1.134	−0.0215	1.13	−0.657	
Pd monolayer[b]	1.73	0.49	1.07	−0.32	−2.021
Pd_2 dimer[b]	0.755	0.175	0.511	−0.24	

[a] These values refer to energy gain/loss due to the particular reaction on a pure gold surface and was used as a reference (zero) for the other alloys, i.e. it was subtracted from the energy calculated for each element for the reaction indicated. [b] The calculations were performed on surfaces where Au (111) was also used as a reference but Pd_2 dimer within the Au(111) surface and a fully covered Au(111) surface by a Pd monolayer were considered.

formation of adsorbed O or OH species, was considered (see Figure 1A−C and Table 2).

As mentioned above, in order to assess the effect of the incorporation of guest metal centers M within the host Au surface, all calculations were referred to the same calculations performed for the pure Au(111) surface. The reactions considered reflect the oxygen reduction pathways described by reactions (I)−(III). The computational strategy involved calculations on the adsorption of the reaction intermediates considered along the pathway leading to H_2O_2 (atop −OO-(ads) and −OOH(ads)) and also dissociation of these intermediates into the −OH or −O adsorbed groups. The effect of the modification of the Au(111) surface by a single transition metal center on O_2 adsorption was described considering the following reaction:

(IV)

where M refers to the transition metal center obtained by replacing a single Au atom within the Au(111) surface and Au represents a gold surface atom within a surface of pure Au(111). Examples of the corresponding slabs with optimized geometry are shown in Supporting Information Figure S1A. The results for all the metals considered are listed in Table 2 (reaction (IV)). A positive value reflects a *stronger* interaction between M and

adsorbed O_2 than that for a Au atom in a Au surface. Dissociation of the O−O bond of this intermediate leading to formation of surface oxides is represented by:

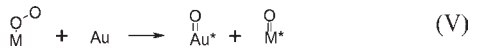

(V)

the asterisk symbol (*) indicates that the oxide is not formed in the atop position but in a three-fold hollow site of the pure or the modified Au(111) surface. For attachment to M*, the oxygen atom is bound by the transition metal atom M and two Au atoms. Examples of the corresponding slabs with optimized geometry are shown in Supporting Information Figure S1B. The results are listed in Table 2, reaction (V), and show that compared with pure Au, the dissociation is not energetically favored for Pd, Pt, and Rh. Another important intermediate of oxygen reduction on gold is the atop HO_2(ads) species, also identified spectroscopically in ref 15. Similarly to reaction (IV), the adsorption on the M metal center is described by:

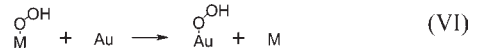

(VI)

The corresponding geometry optimized slabs are shown in Supporting Information Figure S1C and the results are listed in Table 2, reaction (VI). The adsorption energies for HO_2 follow the same trends as O_2 adsorption. The dissociation of the −OOH(ads) intermediate is described by:

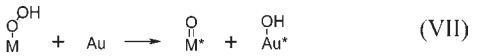

(VII)

The corresponding results are given in Table 2, reaction (VII). Only Pt and Pd show a more favorable behavior compared with gold. The interaction of H_2O_2 with the catalytic surface is weak and similar to that of H_2O, thus, H_2O_2 can be considered as a leaving group. This assumption is supported by the spectroscopic observations on Au where no adsorbed H_2O_2 has been detected.[15]

The binding energy of an O_2 molecule and of the HO_2 intermediate to the guest metal center is, in all cases, significantly higher than that for Au (Figure 1C). Therefore, these alloys improve the 'sticking' of O_2 and HO_2 on the catalyst surface. This is an important result that implies an increase in the O_2 surface adsorption probability related to guest atom locations on the surface.[22,23] Thus, a transition metal atom surrounded by Au creates a *local catalytic center* that has properties different from those of the bulk metal.[34] The main criterion for the selection of the alloying transition metal to increase the production of peroxide has been to consider the energy feasibility of a decomposition channel resulting in O−O bond breaking with the corresponding formation of adsorbed oxygen or hydroxide.

The comparison shown in Figure 1C indicates that three alloying elements have the most promising properties for H_2O_2 electrosynthesis, that is, the least favored O−O dissociation reaction: Pt, Pd, and Rh. A detailed analysis of the kinetics of the oxygen reduction reaction as discussed, for example, for Ni(100),[35] is outside the scope of this work, but the present results provide a clear indication that the further reduction reaction of peroxide to water compared with the behavior on Au is endothermic for these three metals. It should be stressed that the analysis discussed is only valid provided the transition metal centers on the Au surface are isolated from each other. If this requirement is not met and a Pd rich phase segregates, the oxygen reaction will proceed along the water channel instead of leading to peroxide, as it has been experimentally observed for pure Pd.[36] To test the consistency of the analysis described above, the calculations were repeated for a Pd monolayer on top of Au(111) as shown in Figure 1D and for two neighboring Pd atoms within the Au(111) surface (Table 2). It is interesting to note that in both cases, O_2 adsorbates form a bridge between two neighboring Pd atoms, a structure that is commonly assumed to represent the crucial intermediate toward H_2O formation according to reaction (II).[14,15,37]

Oxygen Reduction on Au−Pd Alloyed Surfaces. The calculations considering reactions (IV)−(VII) were also performed for two adjacent Pd atoms within the Au(111) surface and Pd monolayer on top of the Au(111) surface. The results shown in Table 2 clearly indicate that in both cases the O_2 reduction channel toward H_2O is favored. This confirms the need to have *dispersed* individual Pd atoms in the Au(111) surface for selective H_2O_2 production. These results agree with previously published theoretical work on ensemble effects on a Au−Pd surface[37] where it was shown that Pd trimers and dimers should be more effective for breaking of O−O bond than a Pd monomer within a Au monolayer on top of Pd(111). The present work justifies these results by extending the analysis to pure gold providing also a comparative study of the properties of other alloying elements. In addition, the method described here offers the possibility of testing predicted trends with experimental results by providing a 'ranking list' of gold-based alloys for H_2O_2 production.

Studying differential properties, that is, changing a host atom (Au) by a guest (transition metal alloying element), allows a comparison of the properties of oxygenated species bound to the guest atom referred to pure Au, and therefore, the influence of thermal, solvent, electric field contributions are semiquantitatively canceled out since these contribute similarly to the reactivities of the alloy and of the pure Au slab models. The cancelation of these contributions is, indeed, the central quality of the model presented here, thus, focusing exclusively on the differential effects resulting from alloying. It should be clearly stressed that it was not our intention to estimate rate constants but to provide guidelines for establishing families of alloys that could be reasonably expected to direct reactivity for oxygen reduction to hydrogen peroxide.

The validity of the presented model is based on assumption that the activation energies for O−O breaking, for example, do not differ significantly for different alloys or will follow similar trends as the calculated energy differences between reactants and products. This is in contrast to the detailed analysis of different reaction pathways as in, for example, ref 38. Indeed, while it is tempting to compute activation energies obtained with Kohn−Sham DFT, the values obtained are often associated with significant uncertainties regarding the validity of the exchange-correlation potential for such extreme conditions as a transition state often represents.[39,40] Hence, it is concluded that the incorporation of kinetics into the model presented here would not serve the purpose of the study, which is to offer a robust means to screen electrocatalytic properties of different alloying elements in Au.

A detailed analysis of different reaction pathways as in, for example, ref 38, was outside the aim of the present work. A proper analysis would require calculations on charged species, which are not covered by the methods employed. The results presented here were obtained by modeling the oxygen reduction

chemistry on nanoparticles using infinite slabs. For nanoparticles, finite size[41] and geometric effects[42] are known to influence their reactivity. The effect of finite-size is in part addressed in the Layer Thickness Convergence section of the Supporting Information by computing the differential reactivity of HOO(ads)-Pd@Au toward the formation of HO(ads)-Au + O(ads)-Pd@Au for two-, three-, and four-layer slabs. Although the results obtained show some dependence of reaction energies with slab thickness, they clearly indicate that HOO(ads) experiences enhanced protection toward splitting into O(ads) + OH(ads) in the case of Pd@Au as compared with pure Au, independently of slab thickness. This shows the robustness of the model employed to size effects and that the observed trend in reactivities of different alloys should be independent of these effects. Nevertheless, it is clear that for real nanoparticulate systems, geometric effects will contribute to the reactivity of Au−M surfaces, as evident from the results in ref 42 for Au−Pd nanoparticles, for example, nanoparticle shape differences due to chemical composition changes will alter the reactivity as well. Yet, the trends in differential reactivities when comparing Au−M to pure Au nanoparticles with equivalent shapes are expected to prevail.

H_2O_2 Decomposition and Surface Oxide Stability for Au−Pd Alloys. Despite the weak interactions of H_2O_2 with the catalyst surface, further reduction of H_2O_2 to give H_2O can represent a serious problem for H_2O_2 production in a fuel cell. Therefore, the possible energy gain from H_2O_2 decomposition to form water and a surface oxide on Au−Pd alloyed surfaces was evaluated (see Table 2, reaction (VIII)). The reduction of H_2O_2 on the dispersed Pd atoms in Au(111) is favored slightly compared to pure gold but is greatly enhanced for a Pd monolayer. A similar trend has also been observed by Li et al. for the dissociation of peroxide on Pd(111) and Au@Pd surfaces.[38] The work in ref 38 focused on the direct synthesis of H_2O_2 and brings an analysis of reaction kinetics by calculating energies of activation for several peroxide decomposition reaction pathways. It is claimed that the H_2O_2 decomposition properties of Au−Pd alloys determine the enhanced selectivity toward H_2O_2 on Au−Pd alloys. However, a comparison with pure gold to demonstrate how the presence of Pd in gold can suppress H_2O_2 decomposition is not presented, and therefore, it is difficult to compare the results in ref 38 with those discussed here. The results of the present work suggest that, when considering H_2O_2 decomposition, little difference between the behavior of pure gold and gold containing Pd monomers would be expected. In addition, the comparison between the properties of different transition metals are generalized and converted into an overall chemical understanding. In this context, it should be considered that the mechanism for H_2O_2 dissociation differs from a peroxide decay channel by electrochemical reduction. If the disproportionation reaction can be regarded as a combination of two simultaneous electron transfer reactions (oxidation and reduction of peroxide, similarly to a corrosion process), protection from losses is offered by electrode polarization.

Since only the O adsorbate is involved in the interactions with the surface for the H_2O_2 decomposition reaction, the results of these calculations can be directly applied to assess the stability of the surface oxide. The results in Table 2, reaction (VIII), indicate that whereas the oxide stability is very similar for pure Au(111) and for a single Pd atom modified Au(111) surface center, much higher oxide stability is evident for a Pd monolayer. This is an important result that implies a different behavior for a Au−Pd surface with different Pd surface ensembles toward surface oxide formation. Whereas a Au surface containing Pd monomers would behave similarly to pure gold, at least Pd trimers are required for its properties to give rise to a Pd surface oxide formation signature resembling that of bulk Pd.

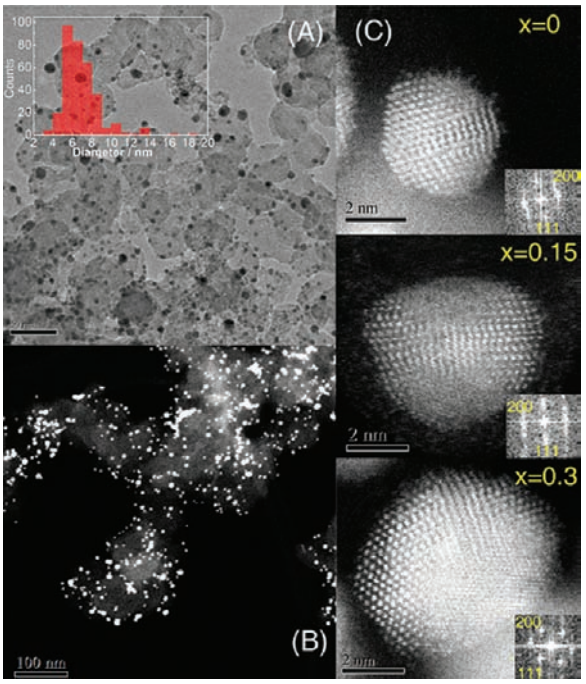

Figure 2. Solid state characterization of $Au_{1-x}Pd_x/C$ materials. (A) HRTEM and (B) HAADF image of $Au_{0.92}Pd_{0.08}/C$; (C) detailed HAADF images of representative particles of $Au_{1-x}Pd_x/C$ with different content of Pd (x); x = 0, 0.15 and 0.3.

Characterization of Au−Pd Nanoalloys. The above prediction regarding the specific reactivity of isolated guest surface atoms was tested for the reduction of O_2 on the Au−Pd system.

The characterization of the nanoalloys is shown in Figures 2 and 3 and Table 1. Transmission electron microscopy (TEM) images indicate good spread of nanoparticles over the carbon support for all preparations (Figure 2A and Supporting Information Figure S2). This was further confirmed by scanning TEM high angle annular dark field (HAADF) images in Figure 2B and Supporting Information Figure S3. Figure 2C shows detailed HAADF images of individual nanoparticles with varying Pd content and the corresponding FFT diagrams show similar orientation along the ⟨110⟩ axis. Lower HAADF contrast intensity was generally observed at the edges of 30% Pd nanoparticles compared to those of pure gold, which likely indicates surface enrichment by Pd (see also Supporting Information Figure S3).[43] Good composition uniformity was confirmed by the similarity of the EDX spectra of individual nanoparticles (Supporting Information Figure S4) and no particles of either pure Pd or Au were detected. The presence of single phase material was also verified from X-ray diffraction (XRD) measurements. The XRD patterns (Supporting Information Figure S5) correspond to an fcc single phase material ($Fd3m$) and no reflections corresponding to pure Au or Pd were observed. The $Au_{1-x}Pd_x$ lattice parameter determined from the XRD patterns follows Vegard's law (Figure 3A) demonstrating alloy formation. The small change of lattice parameters between bulk Au and the Au nanosolids indicates that size induced strain is of secondary importance in this case. The average particle size

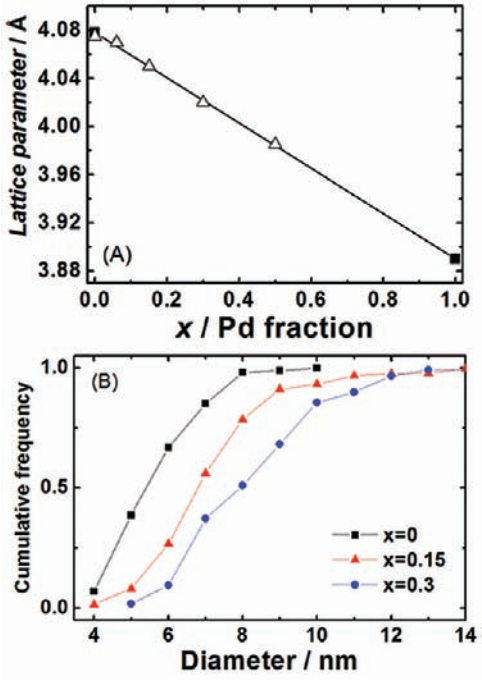

Figure 3. XRD and TEM analyses results. (A) Lattice parameter as a function of palladium content x; (B) cumulative distribution plots for particle size diameters of materials with various x.

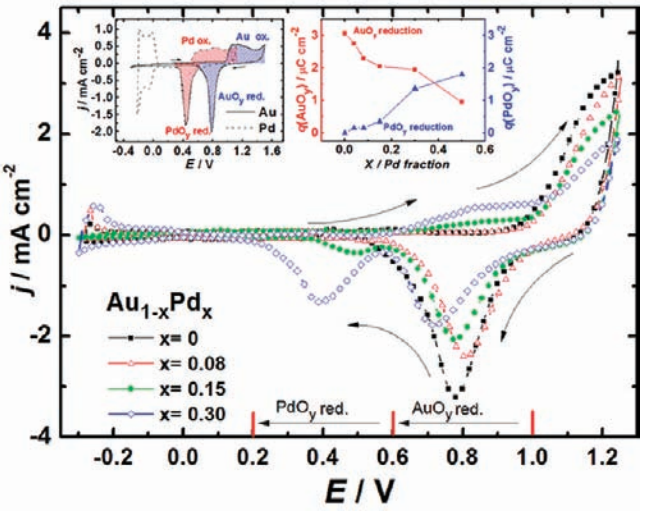

Figure 4. Cyclic voltametry (CV) on $Au_{1-x}Pd_x$/C nanoalloys in Ar saturated 0.1 M $HClO_4$. CVs of pure Au and Pd recorded under the same conditions as in the inset on the left and charge corresponding to reduction of Pd(rich)O_y and Au(rich)O_y calculated by integration within the regions indicated in the Figure as a function of overall palladium content x in the inset on the right. Sweep rate = 200 mV s^{-1}.

determined from XRD peak broadening is in good agreement with the TEM results (Figure 2A and Supporting Information Figure S2) confirming also good particle size monodispersity (Table 1).[17] The Pd/Au ratio was determined by ICP analysis. As expected, the total metal/carbon loading increases slightly with increasing Pd content (Table 1). The cumulative size distribution is shifted to higher values with increasing Pd content due to the increase in particle size resulting from Pd deposition (Figure 3B). The average thickness of the electrocatalytic layer was 1 μm for all the materials investigated. Details of alloy loading are given in Table 1.

The surface electrochemical properties of Au−Pd nanoalloy electrodes were investigated by cyclic voltammetry (CV) and typical results for electrodes prepared with $Au_{1-x}Pd_x$/C particles with increasing Pd content are illustrated in Figure 4. For comparison purposes, the inset to this Figure shows the cyclic voltammograms for bulk Au and Pd electrodes. Clearly distinguishable peaks associated with the formation and reduction of the corresponding surface oxides are observed. The reduction peaks show the pronounced difference in the electrochemical stability of PdO_y and AuO_y surface oxides, of approximately 0.4 V. Thus, the electrochemical oxidation and reduction features of the nanoalloy surfaces can be used as a simple analytical tool to establish the elemental surface population and obtain information on possible surface phase segregation. Pd oxide formation is observed only for $x \geq 0.15$ indicating surface segregation of a Pd rich phase for $x \geq 0.15$. For $x < 0.15$, however, no Pd oxide formation was detected and it can be concluded that these surfaces are either composed of pure Au or contain dispersed Pd atoms within the Au surface. The latter is strongly supported by the observed deviation difference of the voltammetric behavior with that of pure Au. These results are in agreement with calculations of segregation energies of Pd in a Au host for bulk phases[44] and nanoparticles,[45] of 0.28 and 0.89 eV/atom. Other studies have proposed Pd surface segregation in Au(111) and that Pd monomers should be formed on 'free' Au(Pd)(111) surface. Adsorption phenomena, however, should alter segregation properties as has been shown for hydrogen[46] and CO adsorption[47] for this surface, in which case, the formation of a contiguous Pd surface should be favored. The results in Figure 4 indicate that, under the experimental conditions employed, Pd surface segregation does not occur for low Pd concentrations ($x < 0.15$) and will only take place for nanoalloys with a higher Pd content.

The formation of oxidized Pd or Au can be quantified by the charge corresponding to the Au and Pd oxide reduction peaks between 1 and 0.6 V and 0.6 to 0.2 V, respectively. The charge ascribed to Au oxide formation decreases with increasing Pd content whereas the charge related to the Pd oxide peak increases (Figure 4). The Pd oxide reduction charge increase, however, starts to appear only for $x \geq 0.15$. The properties of the surface oxide formed at Pd atom surrounded by Au will be different from those of pure Pd. The potential range used for the CV characterization of the Au−Pd nanoalloys in Figure 4 prevents subsurface oxide formation and the corresponding drastic perturbation of the surface as previously observed experimentally for Au[48] and Pt.[49] Thus, OH adsorption or subsequent adsorption of oxygen should take place in the three-fold hollow position in agreement with the DFT model presented for the Au(111) surface (Supporting Information Figure S1B). The result of calculations of surface oxide stability presented above suggest that the dilute alloy should show similar oxidation behavior to that observed for pure gold in Figure 4. Therefore, it would be expected that a Au rich surface with a minority of Pd atoms will behave similarly to pure Au. This provides support for the argument that a surface alloy containing dispersed Pd atoms is formed for $x < 0.15$ since only contiguous Pd atoms at the surface will lead to the characteristic oxide reduction signature. In addition, the above analysis shows that cyclic voltammetry can be used as a sensitive in situ technique to determine the

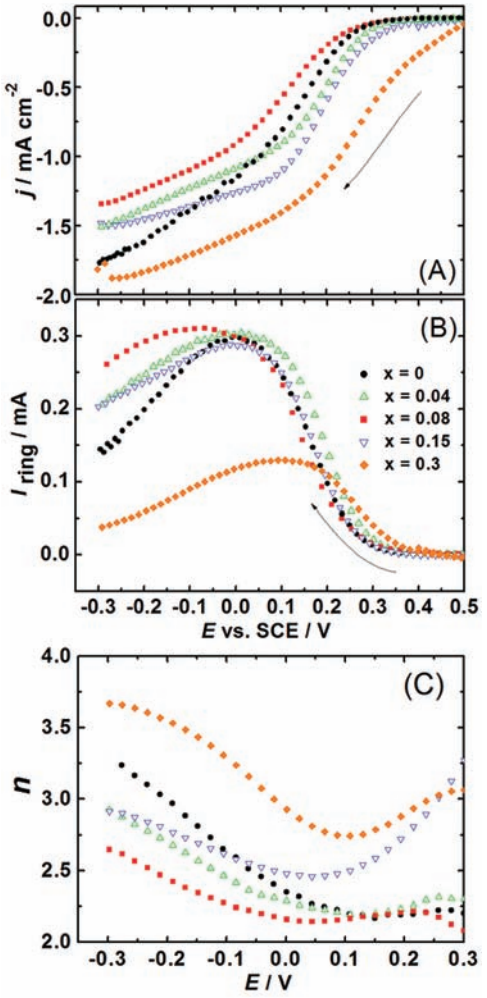

Figure 5. O_2 reduction results obtained on $Au_{1-x}Pd_x/C$ electrodes in O_2 saturated 0.1 M $HClO_4$. (A) Polarization curves at 200 rpm, (B) simultaneous H_2O_2 detection at the ring, (C) and calculated values of *n*. Sweep rate =10 mV s^{-1}; the assignments of the symbols to the actual Pd content, *x*, are indicated in the panel B.

chemical composition of the nanoalloy surface and provides strong evidence for Pd surface segregation for $x \geq 0.15$.

Oxygen Reduction on Au−Pd Nanoalloys. The main in situ technique to ascertain the incorporation of individual transition metal guest sites on the gold surface is to investigate the corresponding response to O_2 reduction and compare these results with those for pure gold. Oxygen reduction was studied on rotating ring-disc electrodes (RRDE) prepared with the different $Au_{1-x}Pd_x/C$ nanoalloys. Electrode preparation and data evaluation was the same as previously described for the Au/C system.[17] Briefly, the H_2O_2 production selectivity was monitored by measuring the reduction currents of O_2 at the disc of the RRDE and detecting the H_2O_2 produced by its quantitative oxidation on the Pt ring.[14] The O_2 reduction selectivity for H_2O_2 formation, $S_{H_2O_2}$, was calculated from $S_{H_2O_2} = (2 \times I_R/N)/(I_R/N - I_D)$, where I_D and I_R are the disc and ring currents, respectively, and *N* is the collection efficiency. The number of electrons exchanged per molecule of O_2 reduced, *n*, was calculated from:[50]

$$n = \frac{4 \times I_D}{I_R/N - I_D} \qquad (2)$$

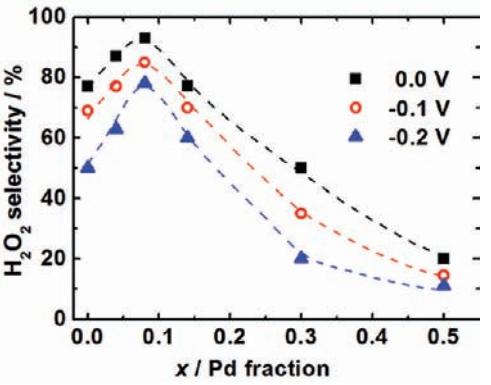

Figure 6. O_2 reduction selectivity toward H_2O_2 production (H_2O_2 selectivity) as a function of palladium content, *x*, at potentials of 0 V (squares), −0.1 V (circles), −0.2 V (triangles). The dashed lines are added to guide the eye.

Figure 5A,B shows oxygen reduction disc currents and the simultaneously measured peroxide oxidation ring currents for different Pd concentrations. The corresponding values of *n* are given in the inset to Figure 5A. It is interesting to notice that the oxygen reduction current below 0.0 V actually decreases as the Pd concentration increases from 0 to 8%. The reason for this effect is the increase in the contribution of peroxide formation with the corresponding decrease in the value of *n*. Both the current and the value of *n* increase for Pd concentrations above 8% in the nanoalloy.

Peroxide selectivity, ($S_{H_2O_2}$), is a more revealing quantity that increases with Pd content up to 8% and then decreases to very low values for higher Pd contents (Figure 6). For all Pd contents, $S_{H_2O_2}$ decreases at increasing negative potentials (Supporting Information Figure S6) due to the further reduction of peroxide. Remarkably, Pd doping up to 8% suppresses the further reduction of H_2O_2 irrespective of the applied potential, thus, sustaining significantly higher H_2O_2 production. The results in Figure 3C indicate that two opposite effects determine the observed O_2 selectivity to peroxide as the composition of the nanoalloys is changed. The DFT modeling and the surface composition analysis by cyclic voltammetry imply that the increase of H_2O_2 selectivity can be directly linked to the incorporation of Pd sites on the Au surface. These act to enhance the rate of peroxide formation compared with that of Au surface atoms due to the enhanced adsorption of O_2 while avoiding O−O bond breaking.

At the other extreme of compositions investigated, increasing the Pd content above 15% triggers surface segregation of Pd rich phases (Figure 4) resulting in an increase in the value of *n* and, hence, in the additional contribution of the water production channel. In this case, reduction of O_2 to water occurs preferentially when the surface contains ensembles of contiguous Pd atoms and not of individual Pd sites within a Au matrix. This leads to a decrease of the H_2O_2 production selectivity down to 10% for a Pd content of 50%. Thus, the balance between local Pd atomic sites and their incorporation within a two-dimensional Pd layer determines the maximum selectivity that can be achieved, which is surprisingly high, reaching values of ca. 95% for an alloy metal fraction of 0.08 as shown in Figure 3B. Similarly to our observations for an electrocatalytic reaction, it is interesting to notice that an analogous maximum was observed by Chen et al.[34] for the heterogeneous chemical catalytic reaction of acetoxylation of ethylene at a surface composition of 0.07 ML of Pd on Au(100).

Since subsurface Pd effects can be ruled out,[23,46] the electrochemical results indicate that individual Pd atoms are present on the alloy surface of the dilute alloys and the resulting greatly enhanced reactivity for peroxide production strongly supports the DFT analysis presented. The applicability of the model system employed in the DFT analysis rationalizes both the observation by Chen et al. on the catalytic promotional effect of gold surrounding individual atoms of Pd[34] and the present results. From the above arguments, the properties of individual Pd atoms present within a Au matrix cannot be linked to the metal electronic structure described by the overall d-band center/width. These observations highlight the 'locality' of catalytic promotion by ensemble effects. Indeed, in terms of the partial d-band density of states (PDOS) projected on the surface, the catalytic centers created by individual Pd atoms within the Au surface can be described by the local PDOS that varies for individual surface atoms[37] (Supporting Information Figure S7). The enhanced sticking of O_2 on Pd reflects the increased atomic d-polarizability of these centers (Supporting Information Figure S7)[23,51] while the surrounding Au atoms ensure weak interactions with the same O_2 molecule. This insight provides a conceptual bridge between monatomic catalytic sites[16] and the dilute adatom metal alloy catalyst. This perspective is complementary to the common electrocatalytic alloy material screening approach based on metal d-band position, mainly suitable for alloys terminated by a single component surface.[20,21]

CONCLUSIONS

A DFT methodology for selecting appropriate metal alloy catalyst for enhanced H_2O_2 production has been presented. It was shown that discrete guest atoms dispersed in a Au host surface will significantly affect reactivity of the surface toward oxygen reduction. The Au surfaces modified by dispersed Pd, Pt, or Rh should display higher H_2O_2 production selectivity than pure gold. Dependence of Pd content in $Au_{1-x}Pd_x$ nanoparticles has been investigated experimentally with respect to the oxygen reduction reaction. A pronounced increase in oxygen reduction selectivity toward H_2O_2 production, approaching 95%, was observed for Pd molar contents of 8%. Further increase of Pd concentration in the nanoalloys leads to losses in H_2O_2 selectivity, which drops below 10% for Pd concentrations of 50%. The enhancement of H_2O_2 production was attributed to the presence of Pd monomers surrounded by gold at the surface of Au−Pd nanoalloys whereas the decrease at Pd concentrations above 15% was due to the presence of contiguous Pd atoms, in agreement with DFT modeling results suggesting that already two adjacent Pd atoms should support H_2O formation instead of H_2O_2. The results presented here correspond to bimetallic nanoparticles composed of very stable elements supported on conducting carbon in the environment of a Nafion film indicating the possibility of their use in proton exchange membrane fuel cells. The importance of the present work is in demonstrating that the concept of individual transition metal centers incorporated within a gold matrix can be utilized to direct reactivity in the electrochemical reduction of oxygen to preferential H_2O_2 production compared with water and that DFT modeling provides a powerful method for material selection. We propose that these results and their extension to other reactions open up the intriguing possibility of an extremely efficient utilization of the Gibbs energy of chemical reactions for the clean cogeneration of electrical energy simultaneously with industrial chemical syntheses. In addition, the approach followed can be extended for alloy selection in the heterogeneously catalyzed direct synthesis of hydrogen peroxide.

ASSOCIATED CONTENT

Supporting Information. Figures S1−S7 and additional calculations. This material is available free of charge via the Internet at http://pubs.acs.org.

AUTHOR INFORMATION

Corresponding Author

jjirkovsky@anl.gov; itai.panas@chalmers.se

Present Addresses

[#]Materials Science Division, Argonne National Laboratory, Argonne, IL 60439, USA.

ACKNOWLEDGMENT

This work has been supported by Solvay R&D, Belgium. In addition, support from the European Union through the ELCAT Marie-Curie Initial Training Network ELCAT, Proposal No. 214936-2, 2008-2012 is gratefully acknowledged.

REFERENCES

(1) Hess, W. T. In *Kirk-Othmer Encyclopedia of Chemical Technology, Vol. 13*, 4th ed.; Kroschwitz, J. I., Howe-Grant, M., Eds.; Wiley: New York, 1995; p 961.
(2) HPPO technology; http://www.basf.com ; http://www.dow.com.
(3) Edwards, J. K.; Solsona, B.; Ntainjua, E.; Carley, A. F.; Herzing, A. A.; Kiely, C. J.; Hutchings, G. J. *Science* **2009**, *323*, 1037–1041.
(4) Stamenkovic, V. R.; Fowler, B.; Mun, B. S.; Wang, G.; Ross, P. N.; Lucas, C. A.; Markovic, N. M. *Science* **2007**, *315*, 493–497.
(5) Yamanaka, I.; Onizawa, T.; Takenaka, S.; Otsuka, K. *Angew. Chem., Int. Ed.* **2003**, *42*, 3653–3655.
(6) (a) Vielstich, W.;, Lamm, A.; Gasteiger, H. A. *Handbook of Fuel Cells, Fundamentals, Technology and Applications*; Wiley: New York, 2003. (b) Hoogers, G. *Catalysts for the Proton Exchange Membrane Fuel Cell*; CRC: Boca Raton, FL, 2003.
(7) Gasteiger, H. A.; Markovic, N. M. *Science* **2009**, *324*, 48–49.
(8) Jirkovsky, J. S.; Busch, M.; Ahlberg, E.; Panas, I.; Krtil, P. *J. Am. Chem. Soc.* **2011**, *133*, 5882–5892.
(9) Edwards, J. K.; Hutchings, G. J. *Angew. Chem., Int. Ed.* **2008**, *47*, 9192–9198.
(10) Tammeveski, K.; Kontturi, K.; Nichols, R. J.; Potter, R. J.; Schiffrin, D. J. *J. Electroanal. Chem.* **2001**, *515*, 101–112.
(11) Wass, R. T. J.; Ahlberg, E.; Panas, I.; Schiffrin, D. J. *Phys. Chem. Chem. Phys.* **2006**, *8*, 4189–4199.
(12) Adzic, R. In *Electrocatalysis*; Lipkowski, J., Ross, P. N., Eds.; Wiley: New York, 1998; Vol. 197.
(13) Kim, J.; Gewirth, A. A. *J. Phys. Chem. B* **2006**, *110*, 2565–2571.
(14) Markovic, N. M.; Gasteiger, H. A.; Ross, P. N. *J. Phys. Chem.* **1995**, *99*, 3411–3415.
(15) Li, X.; Gewirth, A. A. *J. Am. Chem. Soc.* **2004**, *127*, 5252–5260.
(16) Durand, R. R.; Anson, F. C. *J. Electroanal. Chem.* **1982**, *134*, 273–289.
(17) Jirkovsky, J. S.; Halasa, M.; Schiffrin, D. J. *Phys. Chem. Chem. Phys.* **2010**, *12*, 8042–8052.
(18) Lueckoff, U. D; Paucksch, H.; Luft, G. *Ger. Offen.* 1992, DE 4127918, A1 19920910.
(19) Edwards, J. K.; Thomas, A.; Carley, A. F.; Herzing, A. A.; Kiely, C. J.; Hutchings, G. J. *Green Chem.* **2008**, *10*, 388–394.

(20) Stamenkovic, V. R.; Mun, B. S.; Mayrhofer, K. J. J.; Ross, P. N.; Markovic, N. M.; Rossmeisl, J.; Greeley, J.; Nørskov, J. K. *Angew. Chem., Int. Ed.* **2006**, *45*, 2897–2901.
(21) Stamenkovic, V. R.; Mun, B. S.; Arenz, M.; Mayrhofer, K. J. J.; Lucas, C. A.; Wang, G.; Ross, P. N.; Markovic, N. M. *Nat. Mater.* **2007**, *6*, 241–247.
(22) Maroun, F.; Ozanam, F.; Magnussen, O. M.; Behm, R. J. *Science* **2001**, *293*, 1811–1814.
(23) Liu, P.; Norskov, J. K. *Phys. Chem. Chem. Phys.* **2001**, *3*, 3814–3818.
(24) Pluntke, Y.; Kibler, L. A.; Kolb, D. M. *Phys. Chem. Chem. Phys.* **2008**, *10*, 3684–3688.
(25) Schafer, P. J.; Kibler, L. A. *Phys. Chem. Chem. Phys.* **2010**, *12*, 15225–15230.
(26) Al-Odail, F. A.; Anastasopoulos, A.; Hayden, B. E. *Phys. Chem. Chem. Phys.* **2010**, *12*, 11398–11406.
(27) Wang, D.; Villa, A.; Porta, F.; Sua, D.; Prati, L. *Chem. Commun.* **2006**, 1956–1958.
(28) Ketchie, W. C.; Murayama, M.; Davis, R. J. *J. Catal.* **2007**, *250*, 264–273.
(29) Delley, B. J. *Chem. Phys.* **1990**, *92*, 508–517.
(30) Delley, B. *J. Chem. Phys.* **2000**, *113*, 7756–7764.
(31) Materials Studio Release Notes, Release 5.0, Accelrys Software, Inc.: San Diego, CA, 2009.
(32) Perdew, J.; Burke, K.; Ernzerhof, M. *Phys. Rev. Lett.* **1996**, *77*, 3865–3868.
(33) Delley, B. *Phys. Rev. B* **2002**, *66*, 1551251–1551259.
(34) Chen, M.; Kumar, D.; Yi, C. W.; Goodman, D. W. *Science* **2005**, *310*, 291–293.
(35) Panas, I.; Sieghbahn, P.; Wahlgren, U. J. *Chem. Phys.* **1989**, *90*, 6791–6801.
(36) Xiao, L.; Zhuang, L.; Liu, Y.; Lu, J.; Abruna, H. D. *J. Am. Chem. Soc.* **2009**, *131*, 602–608.
(37) Ham, H. C.; Hwang, G. S.; Han, J.; Nam, S. W.; Lim, T. H. *J. Phys Chem. C* **2009**, *113*, 12943–12945.
(38) Li, J.; Staykov, A.; Ishihara, T.; Yoshizawa, K. J. *Phys. Chem. C* **2011**, *115*, 7392–7398.
(39) Lundin, A.; Panas, I.; Ahlberg, E. *J. Phys. Chem. A* **2007**, *111*, 9080–9086.
(40) Busch, M.; Ahlberg, E.; Panas, I. *Phys. Chem. Chem. Phys.* **2011**, *13*, 15062–15068.
(41) Panas, I.; Schüle, J.; Siegbahn, P. E. M.; Wahlgren, U. *Chem. Phys. Lett.* **1988**, *149*, 265–272.
(42) Ham, H. C.; Hwang, G. S.; Han, J.; Nam, S. W.; Lim, T. H. *J. Phys. Chem. C* **2010**, *114*, 14922–14928.
(43) Ferrer, D.; Blom, D. A.; Allard, L. F.; Mejia, S.; Perez-Tijerinacd, E.; Jose-Yacaman, M. *J. Mater. Chem.* **2008**, *18*, 2442–2446.
(44) Ruban, A. V.; Skriver, H. L.; Nørskov, J. K. *Phys. Rev B* **1999**, *59*, 15990–16000.
(45) Wang, L.-L.; Johnson, D. D. *J. Am. Chem. Soc.* **2009**, *131*, 14023–14029.
(46) Venkatachalam, S; Jakob, T. *Phys. Chem. Chem. Phys.* **2009**, *11*, 3263–3270.
(47) Soto-Verdugo, V.; Metiu, H. *Surf. Sci.* **2007**, *601*, 5332–5339.
(48) Bruckenstein, S.; Shay, M. *J. Electroanal. Chem.* **1985**, *188*, 131–136.
(49) Bjorling, A.; Ahlberg, E.; Feliu, J. M. *Electrochem. Commun.* **2010**, *12*, 359–361.
(50) Bard, A. J.; Faulkner, L. R., *Electrochemical Methods—Fundamentals and Application*; Wiley: New York, 2001.
(51) Panas, I.; Siegbahn, P.; Wahlgren, U. *Chem. Phys.* **1987**, *112*, 325–337.